1-23-2017

One Ion to Rule Them All: Combined Antibacterial, Osteoinductive and Anticancer Properties of Selenite-Incorporated Hydroxyapatite

Vuk Uskoković
Chapman University, uskokovi@chapman.edu

Maheshwar Adiraj Iyer
The University of Illinois at Chicago

Victoria M. Wu
Chapman University

Recommended Citation

Uskoković V, Iyer MA, Wu VM. One ion to rule them all: the combined antibacterial, osteoinductive and anticancer properties of selenite-incorporated hydroxyapatite. *J Mater Chem B Mater Biol Med.* 2017;5(7):1430–1445. doi:10.1039/C6TB03387C

One Ion to Rule Them All: Combined Antibacterial, Osteoinductive and Anticancer Properties of Selenite-Incorporated Hydroxyapatite

HHS Public Access

Author manuscript

J Mater Chem B Mater Biol Med. Author manuscript; available in PMC 2018 January 23.

Published in final edited form as:

J Mater Chem B Mater Biol Med. 2017 ; 5(7): 1430–1445. doi:10.1039/C6TB03387C.

One Ion to Rule Them All: Combined Antibacterial, Osteoinductive and Anticancer Properties of Selenite-Incorporated Hydroxyapatite

Vuk Uskoković[1,2,*], **Maheshwar Adiraj Iyer**[2], and **Victoria M. Wu**[1,2]

[1] Advanced Materials and Nanobiotechnology Laboratory, Department of Biomedical and Pharmaceutical Sciences, Chapman University, Irvine, CA 92618-1908, USA

[2] Advanced Materials and Nanobiotechnology Laboratory, Department of Bioengineering, University of Illinois, Chicago, IL 60607-7052, USA

Abstract

Although hydroxyapatite (HAp) has been doped with dozens of different ions, the quest for an ion imparting a combination of properties conducive to bone healing is still ongoing. Because of its protean potency and the similarity in size and shape to the phosphate tetrahedron, selenite ion presents a natural ionic substitute in HAp. The incorporation of selenite into synthetic HAp using two different methods – co-precipitation and ion-exchange sorption - was studied for its effect on crystal properties and on a triad of biological responses: antibacterial, anticancer and osteoinductive. Co-precipitation yielded HAp with higher selenite contents than sorption and the stoichiometry of HAp richest in selenite was represented as $Ca_{9.75}(PO_4)_{5.75}(SeO_3)_{0.25}(OH)_{1.75}$. Crystallinity of HAp decreased in direct proportion with the amount of selenite incorporated. Because of their lower selenite content, HAp powders prepared by ion-exchange exhibited a consistently higher crystallinity compared to the co-precipitated ones. Annealing partially recovered the crystallinity, yet the difference in crystallinity between powders prepared by co-precipitation and by ion-exchange remained, suggesting that the amorphization is mainly due to structural incorporation of selenite, not its effect on the crystal growth kinetics. The addition of selenite changed the morphology of HAp nanoparticles from acicular to rounded and affected the crystal lattice parameters in different ways depending on whether the powders were annealed or not. As for the annealed powders, the incorporation of selenite contracted the lattice in both *a* and *c* crystallographic directions. In the agar diffusion assay, the effectiveness of HAp was more dependent on the presence or absence of selenite in it than on its concentration and was highest against *E. coli* and *S. aureus,* moderately high against *S. enteritidis* and ineffective against *P. aeruginosa*. In liquid inoculation tests, on the other hand, the antibacterial activity of HAp was directly proportional to the amount of selenite contained in it. The viability of K7M2 osteosarcoma cells decreased in direct proportion with the amount of selenite in HAp and was significantly different from the untreated control and from pure HAp at contents equal to or higher than 1.9 wt.%. In contrast, no reduction was observed in the viability of primary fibroblasts treated with HAp incorporating different amounts of selenite ions, suggesting their potentially selective anticancer activity: lethal for the cancer cells and harmless for the healthy cells. Finally, mRNA

[*]Corresponding author; vuk21@yahoo.com, uskokovi@chapman.edu.

expression of bone gamma-carboxyglutamate protein (BGLAP3) was higher in differentiated MC3T3-E1 osteoblastic cells treated with selenite-incorporated HAp particles than in cells treated with pure HAp. The osteoinductive effect was due to an overall higher metabolic activity of cells treated with the particles and not due to increased proliferation. In such a way, a triad of antibacterial, osteoinductive and anticancer activities was attributed to selenite-incorporated HAp.

1. Introduction

Being the mineral component of vertebrate hard tissues, hydroxyapatite (HAp) is naturally compatible with the biological systems, making it a material of choice for hard tissue engineering. Tissue engineering constructs have been generally designed as composites containing a polymeric phase and HAp[1], but thanks to its viscous properties in the cement form[2], HAp has been often used alone as a bone graft in maxillofacial and orthopedic surgeries[3]. It has also been used as a support structure in scaffolds owing to its large compressive strength[4] as well as an osteoconductive component that promotes bone remodeling and regeneration[5].

HAp is a versatile solid, capable of augmenting tissue engineering constructs with multiple other functionalities. A particularly popular application of HAp is as a drug carrier[6] to deliver drugs such as bisphosphonates[7], antibiotics[8] and other antimicrobial agents[9,10], anticancer chemotherapeutics[11,12], *et cetera*. HAp also possesses a rare form of stoichiometric flexibility, given that its crystal structure can maintain the characteristic $P6_{3/m}$ symmetry within a broad range of Ca/P molar ratios (1.3 – 2) and under a very high concentration of defects. This allows HAp to be doped with a wide range of chemical elements and groups. It was being reported that more than half of the elements of the Periodic Table could be incorporated inside HAp[13]. The use of HAp as a hard component of tissue engineering constructs has thus naturally progressed into a school of thought that advocates the incorporation of one or multiple types of ions into HAp and the adjustment of the stoichiometric composition so as to impart novel properties. Mg-HAp, for example, promoted mineralization as a coating on Ti implants more effectively than pure HAp[14] and was also observed to possess a more osseointegrative nature than native HAp[15], presumably owing to its increased resorption rate. Bone cell viability following incorporation of Co and Mn ions into HAp structure were also comparable to native HAp[16]. Mn was further reported to be beneficial for bone regeneration due to its induction of osteoblast proliferation and the propensity to positively influence the osteoblast metabolic activity[17]. Incorporation of Fe into HAp crystal structure to impart magnetic properties to the material[18] and the resulting promotion of bone remodeling and tissue regeneration have also been reported[19]. Further, Fe-doped HAp has also been exploited for its superparamagnetic nature[20] as well as to deliver drugs[21] and boost the osteoblastic activity[22], thus positively affecting bone regeneration. Cobalt-incorporated HAp has been shown to favor osteogenesis *in vivo*[23], while also demonstrating an antibacterial activity[24]. A more extensive bone ingrowth and an improved bone tissue coverage of the implant have also been reported for Si-containing HAp[25]. HAp with the trace amounts of Ag ions was demonstrated as favorable as an antibacterial nanomaterial for dental and orthopedic implants[26]. Similar antibacterial activities were reported for Ce- and Eu-doped HAp[27,28]. The use of Sr as a dopant has been

justified by its well-known affinity toward bone and a potential therapeutic use in mitigating osteoporosis by enhancing the formation of new bone[29]. CO_3^{2-} substitution of the PO_4^{3-} group has been reported to enhance the bio-integration of HAp implants when studied in white rabbits[30]. Most recently, doping HAp with Hf endowed it with the ability to produce large concentrations of reactive oxygen species under ionizing radiation and made it a candidate for materials for photodynamic antitumor therapies[31]. However, although HAp has been doped with dozens of different ions in search of the perfect ionic substitute, the quest for an ion imparting a versatile combination of properties conducive to the bone healing process is still ongoing. In this study, we investigate an oxyanion of selenium for one such synergistic effect.

Once considered a toxic element, selenium (Se) is now known to be an essential micronutrient involved in various metabolic processes[32]. For example, it is a part of selenoenzymes, which prevent and reverse the oxidative damage, enabling Se to even act as an antidote against potent toxins, including mercury[33]. Not only does it possess pronounced antibacterial properties[34] and is a potent antioxidant and chemopreventive agent in oncology[35], but it also has a pronounced effect on bone development. For example, its deficiency inhibited bone growth[36]; its concomitant dosing with anastrazole prevented resorption and other symptoms of bone toxicity[37]; and its vitamin-supplemented administration to osteoporotic white rabbits restored the trabeculae density to a normal state[38]. Because of this protean potency, which makes it fundamentally similar to HAp in many respects[39], as well as the almost identical size as the phosphate tetrahedron, selenite ion, SeO_3^{2-}, presents a natural ionic substitute in HAp (Fig.1). Previous studies have shown that SeO_3^{2-} incorporates well into HAp crystals and that it need not result in the formation of a separate phase[40]. The antibacterial activity of SeO_3^{2-} ions also increased following their incorporation into HAp[41]. Even at the low weight content of 0.6 %, SeO_3^{2-} ions in HAp inhibited *P. aeruginosa* and *S. aureus* from establishing biofilm[42]. Biocompatibility and the antibacterial activity of selenite-containing HAp (Se-HAp) could be utilized against biofilm formation on implants, which is a major source of infection following surgical implantation[43,44]. An immediate benefit of this approach would be reduced dependence of patients on strong antibiotics for prophylactic purposes. The incorporation of SeO_3^{2-} into HAp has also been demonstrated to have a therapeutic effect against hepatocellular carcinoma *in vivo*[45]. Specifically, while the tumor volume and mass failed to be reduced four weeks after the intravenous injection of Se-HAp, the survival rate of treated vs. untreated mice differed significantly. The animals treated with Se-HAp had a 100% survival rate over a 36-day period compared to the untreated ones (55 %) and those treated with pure HAp (78 %). On top of being able to stop the progression of malignant tumors, Se clusters deposited on titania promoted the proliferation of healthy osteoblasts[46,47], suggesting the potentially selective anticancer and osteogenic behavior of the oxyanions of this metal, which we have explored in this study. In total, we have followed the effects of SeO_3^{2-} ions on the crystallinity and the crystal growth habit of HAp as well as on the antibacterial, osteoinductive and anticancer effects of selenite-doped HAp (Se-HAp) *in vitro*.

2. Materials and methods

2.1. Preparation of HAp and selenite-containing HAp powders

To synthesize HAp, 88 ml of 0.1 M $Ca(NO_3)_2$ and 94 ml of 0.06 M $(NH_4)_2HPO_4$ were mixed and 18 ml of 1 M NH_4OH was added to the reaction mixture, which was then heated to 65 °C and maintained for an hour. To account for the later inclusion of selenite ions, Ca/P molar ratio in the solution from which HAp was precipitated was 1.56, lower than 1.67 typifying stochiometric HAp. The formed suspension was allowed to cool at room temperature, before it was washed with deionized water. Prior to washing and after washing the precipitate was separated from the supernatant by centrifugation at 5000 rpm for 5 min. The precipitate was then dehydrated overnight in a vacuum oven at 80°C to obtain dry HAp powder.

Selenite-incorporated HAp (Se-HAp) was prepared using two different methods: (1) co-precipitation and (2) post-precipitation, i.e., ion-exchange sorption. To make co-precipitated Se-HAp, varying amounts of sodium selenite were added to $(NH_4)_2HPO_4$ solution so as to cover the 0 – 25 wt.% range with respect to the weight of HAp ionic components in the solution from which HAp was precipitated. The synthesis procedure was otherwise identical to that yielding pure HAp. Post-precipitation synthesis of Se-HAp incorporation was achieved by immersing the precipitated HAp powder in a sodium selenite solution (pH ~ 10) in concentrations in the range of 10 to 40 %w/w with respect to the weight of the solid phase for 48 h. The powders were washed with distilled water to eliminate the excess unbound selenite and dried as described above. The as-precipitated and dried powders were annealed at 800 °C for 3 h in a horizontal tube furnace (Acros International, STF1200) in air.

2.2. Physicochemical characterization

X-ray diffractometry was carried out on a Bruker D2 Phaser diffractometer and on powders pre- and post-annealing using 10 – 90 ° 2Θ range, the step size of 0.002°, and the scan time of 1.5 s/step. The average crystallite size was determined from the Scherrer equation using Diffrac.Eva XRD analysis software. Crystallinity of the powders (X_c) was calculated using the following relation, in which $V_{112/300}$ is the intensity of the trough between the (112) and (300) reflections and I_{300} is the intensity of the (300) reflection[48]:

$$Xc=1-\left(\frac{V_{\frac{112}{300}}}{I_{300}}\right) \quad \text{(Eq. 1)}$$

Interplanar spacing (d_{hkl}) was measured using the Bragg relation where λ is the wavelength of Cu K_α radiation, 1.5418 Å, and Θ is the diffraction angle for (hkl) reflection:

$$d_{hkl}=\frac{\lambda}{2sin\,\Theta_{hkl}} \quad \text{(Eq. 2)}$$

The hexagonal lattice parameters of HAp, *a* and *c*, were calculated from d_{hkl} using the following equation:

$$\frac{1}{d^2}=\frac{4}{3}\left(\frac{h^2+hk+k^2}{a^2}\right)+\frac{l^2}{c^2} \quad \text{(Eq. 3)}$$

Transmission Electron Microscopy (TEM) studies were performed on a JEOL JEM 1220 Life Science TEM operated at 80 kV. Inductively Coupled Plasma Mass Spectroscopy analysis was carried out at the Microanalysis Facility at the University of Illinois at Urbana-Champaign.

2.3.Antibacterial assays

Annealed Se-HAp powders were tested for their antibacterial activity against Escherichia coli, Staphylococcus aureus, Staphylococcus epidermis, Salmonella enteritidis, and *Pseudomonas aeruginosa* using the agar diffusion and liquid inoculation assays. Ten mg of the powder were placed onto a bacterium-infused nutrient agar plate with the spot radius of 1 cm. The powders were deposited as a paste by adding minute volumes (20 μl) of water to them and mixing well so that they did not spread while spotting. The plates were then allowed to incubate for 24 - 48 h at 37 °C. The zone of inhibition was used to gauge the antibacterial activity of the powders depending on their selenite content. Pure, Se-free HAp and vancomycin-loaded Se-HAp were used as negative and positive controls, respectively. All the samples for this assay were analyzed in triplicates. In the liquid inoculation test, a single colony of *S. aureus* cultured on a blood agar plate over a period of 24 h was stabbed with a pipette tip, placed in 5 ml of brain heart infusion broth (*Sigma Life Sciences*) containing 5 mg/ml Se-HAp, and incubated overnight at 37 °C and 170 rpm. The same procedure was repeated for *E. coli*. All the samples for this assay were analyzed in duplicates.

2.4. Anticancer studies

A viability assay was run using Vybrant MTT Cell Proliferation Assay Kit (Molecular Probes Inc.). K7M2 murine osteosarcoma cells (ATCC) were seeded at 5,000 cells/well in a Falcon 96-well plate and allowed to incubate for 48 h. Nanoparticles were then added at 2 mg/ml and allowed to incubate for another 48 h. The MTT proliferation assay was run according to the Vybrant MTT Cell Proliferation Assay Kit protocol. Media were removed from each well and replaced with 100 ml of fresh media, along with 10 μl of 12 mM of MTT stock solution. The cells were incubated at 37 °C for 4 h. At the conclusion of the incubation, all but 25 μl of media were removed from each well, followed by the addition of 50 μl of DMSO. Each well was stirred and the plate was allowed to incubate for 10 min. After the incubation, absorbance was read at 540 nm using a FLUOstar Omega microplate reader (BMG LabTech). To estimate cell viability, absorbance values were normalized to the difference between the absorbance of untreated negative controls and the absorbance of the pure medium. All the samples were analyzed in triplicates. The same test was performed on mouse primary lung fibroblasts isolated from 9 week old C57B6/J mouse lungs.

Immunofluorescent studies were performed on the same two types of murine cells: K7M2 and primary lung fibroblasts. The cells were fixed and stained for nucleus, f-actin, and HAp.

They were fixed for 5 minutes in 4 % paraformaldehyde (PFA) and washed 3 × 10 min in phosphate buffered saline (PBS). Alexa Fluor 568 phalloidin (1:400) and OsteoImage reagent (1:100) were then added and incubated for 1 hour at room temperature. After the incubation, the cells were washed 3 × 5 min with OsteoImage wash buffer. Cells were then incubated in NucBlue® Fixed Cell ReadyProbes™ reagent (Molecular Probes, Life Technologies) for 5 - 10 min, rinsed in PBS and mounted on glass slides. Images were acquired on a Zeiss LSM 710 confocal microscope (UIC core imaging facility).

2.5. Osteoinductivity assay

Mouse calvarial preosteoblastic cell line, MC3T3-E1 subclone 4, was purchased from American Tissue Culture Collection (*ATCC*, Rockville, MD). The cells were seeded at 1.5×10^5 cells/well in 24 well plates and cultured in 1 ml of Alpha Minimum Essential Medium (α-MEM; *Gibco*) supplemented with 100 ug/ml ascorbic acid and 10% fetal bovine serum (FBS, *Invitrogen*). After 17 days of incubation, the suspension containing 5 mg/ml of particles was added to the cells and incubated for 72 h. After the given time, cell lysis, reverse transcription (*Bio-Rad*) and qPCR (*Applied Biosystems, StepONEPlus*) were performed using the Taqman kit (*Applied Biosystems*) in accordance with the manufacturer's instructions. At the same time point, mineralized particles were stained with alizarin red by incubating the cells with it for 15 min. This was followed by fixation using a 15-minute treatment with 10 % paraformaldehyde (PFA) and washing repeatedly with water in-between the steps. Each experiment was done in duplicates and each experimental replica was analyzed for mRNA expression in triplicates ($n = 2 \times 3$). The real-time PCR data were analyzed using the $\Delta\Delta C_t$ method[49].

2.6. Statistical analysis

All biological experiments were conducted in triplicates unless noted otherwise and the results are expressed as means +− standard deviation ($n \geq 3$). Student's t-test was used to estimate the statistical significance ($p < 0.05$) of difference between sample and control data points.

2.7. Ethics of animal experimentation

Complying with the federal regulations of animal research, animal experimentation protocols were approved by the Office of Animal Care and Institutional Biosafety (OACIB) at the University of Illinois at Chicago (UIC).

3. Results and Discussion

3.1. Physical characterization of Se-HAp

Selenite-incorporated HAp powders (Se-HAp) were synthesized in this study by two different methods: (1) co-precipitation and (2) ion exchange sorption, aka post-precipitation. On one hand HAp is used by the body as a mineral reservoir owing to its ability to easily undergo ionic substitutions and accommodate a variety of differently sized and charged ionic species, while on the other hand HAp has been used with success as an adsorbent in chromatographic columns[50,51], gas sensors[52] and environmental purification technologies[53,54,55]; hence the rationale for testing both of these methods for the capture of

selenite ions. Sorption of selenite proceeds by substituting phosphate groups on the surface of HAp[56], yet in the case of co-precipitation the additional possibility for the bulk incorporation of selenite is likely to produce a higher ion incorporation efficiency. This expectedly lower level of incorporation of selenite ions into HAp via surface sorption than via co-precipitation was confirmed by the compositional analysis, the results of which are shown in Fig.2. In both cases, only a portion of dissolved SeO_3^{2-} ions entered the HAp lattice. The highest achieved weight content of selenite was close to 3 wt.% for the co-precipitated powders compared to ten times less (0.36 wt.%) for the post-precipitated ones, proving that SeO_3^{2-} incorporation in co-precipitated powders is not limited to surface adsorption/complexation or ion exchange, but is majorly tied to substitution of phosphates in the interior of the particle. This range of selenite contents from 0.3 – 3 wt.% corresponds to the phosphate-to-selenite conversion ratios of 0.6 – 4.7 %. Technically, approximately one in 20 phosphate groups gets substituted with selenite at the highest amount of incorporation. The stoichiometry of the resulting Se-HAp could be tentatively represented as $Ca_{9.75}(PO_4)_{5.75}(SeO_3)_{0.25}(OH)_{1.75}$ if we were not to take into account the inevitable presence of carbonate ions at phosphate sites too, typically yielding $(CO_3)_x$ with $0.1 < x < 0.4$.

The change in size and morphology of HAp particles following incorporation of selenite is seen from TEM images (Fig.3). Annealed HAp is a mixture of ~ 5 nm sized spheres and particles acicular in shape, having the length of 50 – 100 nm and the width of 10 – 15 nm (Fig.3a). The coexistence of these two types of particles is indicative of the aggregational crystal growth that is characteristic for HAp[57]. Elongated morphologies are typical for HAp and result from its crystallographic tendency to grow faster along its hexagonal c-axis than in the directions parallel to the basal plane. However, with the incorporation of selenite, this tendency is lost and the particles gain a more isotropic shape, with sizes in the 20 – 50 nm range (Fig.3b). It is possible that SeO_3^{2-} interferes with the aggregation of smaller, spherical and poorly crystalline primary HAp particles into more crystalline needles, as the result of which the crystallinity of Se-HAp is lower than that of HAp (EDS not shown). Although an increase in the heat content of the system usually favors the elongation of HAp particles[58,59], such a tendency was hampered by the crystallographic effects of phosphate-to-selenite substitution.

X-ray diffractograms of the synthesized HAp powders, both pure and selenite-doped, are shown in Figs.4-5. No samples comprised a separate selenite phase and they were all monophasic with the exception of the annealed Se-HAp with the highest amount of incorporated SeO_3^{2-}, displaying the additional presence of calcium pyrophosphate (β-$Ca_2P_2O_7$). Per Eq.3, as SeO_3^{2-} content in HAp increases, so does Ca/P molar ratio increase, favoring the precipitation of an additional phase. Diffraction peaks of pristine HAp broaden due to the incorporation of the SeO_3^{2-} ion in place of the PO_4^{3-} ion and the crystallinity of co-precipitated powders is inversely proportional to the SeO_3^{2-} content. In an aforementioned study by Kolmas *et al.*[41], the decrease in crystallinity paralleling the incorporation of SeO_3^{2-} into HAp by co-precipitation using the same reactants as in our method was apparent, but less pronounced. In other studies[60,61], on the other hand, the effect of diminished crystallinity was equally intense as that reported here. This amorphization effect might be closely tied to the incongruency of ion transfer at the HAp/solution interface.

First of all, HAp is typified by incongruent dissolution, releasing more Ca^{2+} than PO_4^{3-} in the acidic milieu and more PO_4^{3-} than Ca^{2+} under alkaline conditions[62]. Conversely, formation of phosphate network is the first step in nucleation of HAp, the reason for which high phosphate and low calcium concentrations favor HAp formation more than the other way around[63] and are routinely used in biomimetic mineralization experiments[64]. As a result, the activation barriers for Ca^{2+} and $H_xPO_4^{x-3}$ ions differ and the crystal growth rate can be twice higher at high $[H_xPO_4^{x-3}]/[Ca^{2+}]$ ratios, even when the supersaturation ratio is the same[65]. The integration of selenite into this strained network of phosphate ions would distort the lattice growing around it and reduce its long-range order. Additionally, it may hinder the proneness of the lattice to dissolution/reprecipitation in a phosphate-rich solution, the mechanism through which the primary amorphous particles ripen into crystalline units. As a result, the HAp structure becomes effectively "frozen" in this transitory amorphous state. The third possible effect might come from SeO_3^{2-} ion solutes in the double charge layer, which may be possible given only a small percentage of SeO_3^{2-} ions that get incorporated into the lattice. In this case, SeO_3^{2-} ions might suppress the Debye screening length and thus reduce the degrees of freedom in the stochastic process of coalescing nanoparticles' seeking the most preferable orientation as they come into contact with each other, randomizing its outcomes and lowering the crystalline order in the system.

In the case of structurally analogous phosphate-to-carbonate substitution, occurring at room temperature and yielding so-called B-type carbonated HAp, the lattice parameter *a* decreases while the lattice parameter *c* increases[66] due to the smaller radius of CO_3^{2-} (178 pm) than that of PO_4^{3-} (238 pm). In spite of the fact that the thermochemical radii of phosphate and selenite ions are almost identical, equaling 238 and 239 pm, respectively, both the lattice parameters *a* and *c* decreased in the annealed powders following phosphate-to-selenite substitution. Thus, as calculated from the 2θ shifts of (300) and (002) reflections shown in Fig.6, at the highest amount of incorporated SeO_3^{2-} ions in annealed Se-HAp, d_{300} equaled 2.717 Å and d_{002} equaled 3.431 Å compared to d_{300} = 2.719 Å and d_{002} = 3.437 Å for pristine HAp (Table 1). The corresponding unit cell dimensions decrease isotropically from a = 9.419 Å and c = 6.874 Å for pure HAp to a = 9.412 Å and c = 6.862 Å for HAp containing 3 wt.% SeO_3^{2-}. This contraction of HAp lattice following SeO_3^{2-} incorporation, observed earlier too[67], can be explained by two effects: a) the flatter shape of trigonal SeO_3^{2-} pyramids than that of PO_4^{3-} tetrahedra; b) the paired Ca^{2+} and OH^- vacancies forming as the result of every phosphate–to-selenite substitution to rebalance the charge, as in accordance with the following equation:

$$Ca_{10}(PO_4)_6(OH)_2 + SeO_3^{2-} \rightarrow Ca_9(PO_4)_5(SeO_3)OH + Ca^{2+} + OH^- + PO_4^{3-} \quad \text{(Eq. 3)}$$

In contrast, as the result of increased interatomic distances consequential to amorphization, the incorporation of selenite in as-precipitated HAp expanded the lattice parameter *c*, as seen from the shift in 2θ value for the (002) diffraction maximum in Fig.6. As also seen from Fig. 6, (300) peak exhibited significant broadening following incorporation of selenite, whereas the effect was noticeable, but significantly less pronounced for the (002) peak. This was corroborated in the TEM analysis of the evolution of the particle morphology as a function

of the selenite content. In other words, the evolution of the crystallite morphology from acicular to round must be due to the impeded growth along the basal plane and not the screw axis of hexagonal crystals. The recovery of crystalline order along the basal plane, i.e. in the [300] axis direction, was only partial following annealing, whereas that along the c-axis of the hexagonal lattice, i.e. in the [002] axis direction, was complete. The diminishment of the crystalline order consecutive to the incorporation of selenite ions was, thus, significantly more pronounced along the basal plane than along the c-axis and paralleled the reduction in elongation of particle shapes as a function of the selenite content.

The crystallite size estimated from the broadening of the most intense, (211) reflection decreased in inverse proportion with the selenite content (Fig.7). All Se-HAp powders, regardless of the formation route, demonstrate this trend. As far as the as-precipitated powders are concerned, this decrease is most intense at the onset of the selenite incorporation, at its lowest weight content, with any further increases in this content leading to little or no change in the crystallite size. This is in contrast to the trend observed for annealed co-precipitated powders, where a successive increase in the selenite content leads to a corresponding drop in the crystallite size. Annealing the co-precipitated powders mitigated this amorphization effect caused by selenite ions only at low SeO_3^{2-} contents (0 – 1.2 wt.%). At higher SeO_3^{2-} contents, however, the decrease in the crystallite size as the function of SeO_3^{2-} content becomes ever more drastic following annealing. Thus, as could be seen from Fig.7a, whereas the average crystallite size estimated from the Scherrer equation drops from 33 to 12 nm as SeO_3^{2-} is added to HAp in 1.2 wt.% for non-annealed co-precipitated powders, it increases from 43 to 52 nm at the same amount of SeO_3^{2-} for the annealed co-precipitated powders. However, while the crystallite size drops by more than 5 times, i.e. from 33 to 6 nm, as SeO_3^{2-} content increases from 0 to 3 wt.% for non-annealed co-precipitated powders, it decreases by more than 4 times, i.e. from 43 to 10 nm for the annealed co-precipitated powders in the same SeO_3^{2-} content range. As far as the annealed powders prepared via ion-exchange sorption are concerned, no significant change in the crystallite size was observed depending on the selenite content. Annealing the post-precipitated powders, in contrast to the co-precipitated ones, also completely mitigated the trend of amorphization caused by selenite ions. As could be seen from Fig.7b, whereas the crystallite size of HAp dropped from 34 to 22 nm as SeO_3^{2-} was added to it in its highest amount for non-annealed post-precipitated powders, it increased from 43 to 48 nm for the annealed post-precipitated powders in the same SeO_3^{2-} content range. Fig.7c-d demonstrates that the crystallite size at identical selenite contents was larger for post-precipitated powders than for co-precipitated ones, be they annealed or not. This is a direct consequence of the ability of selenite to incorporate itself in the bulk of the nanoparticles only when it is co-precipitated together with Ca^{2+}, PO_4^{3-} and OH^- ions. Selenite incorporates into the co-precipitated powders during the formation of the crystal and becomes isotropically distributed throughout the crystal lattice, as opposed to its surface substitution of phosphates in post-precipitated powders. For this reason, the effect of selenite on HAp properties is more pronounced for co-precipitated powders.

With the difference in the anionic size being negligible between phosphate and selenite, the lattice strain and its effects on crystallinity must be due to the coupled Ca^{2+} and OH^- vacancies in the lattice forming as the result of the need to compensate the substitution of

trivalent phosphate with divalent selenite. Another reason why the crystallinity of HAp diminishes in direct proportion with selenite content may come from the effect of SeO_3^{2-} ion on nucleation and crystal growth of HAp. It was observed that the admixtures containing 17.0 and 22.7 wt.% of selenite tend to precipitate even without the addition of the base, suggesting the ability of SeO_3^{2-} ion to act as a nucleation promoter, thus increasing the nuclei density and decreasing the size of the final crystallites. In contrast, at lower selenite contents (5.6 and 11.3 wt.%), the solutions containing Ca^{2+} and $H_xPO_4^{x-3}$ required the addition of a base to increase the pH and drive the precipitation reaction to completion.

The amorphization of HAp as the result of incorporation of selenite ions is further seen from the consistently lower crystallinity of the co-precipitated powders than the post-precipitated ones, as estimated from Eq.1 (Fig.8). Annealing partially recovers the crystallinity, but retains the same level of difference in crystallinity between the co-precipitated and the post-precipitated powders (Fig.8). This indicates that the amorphization is mainly due to structural effects, not the crystal growth effects. The way selenite gets incorporated in the lattice is more critical in explaining this effect than its possible modification of the crystal growth kinetics.

3.2. Biological characterization of Se-HAp

3.2.1. Antibacterial activity of Se-HAp—Results of the blood agar assay are presented in Fig.9 as inhibition zone diameters vs. selenite content in Se-HAp for four types of bacteria - *E. coli*, *S. aureus, S. enteritidis and P. aeruginosa* - and four types of samples: co-precipitated Se-HAp, post-precipitated Se-HAp, co-precipitated Se-HAp loaded with vancomycin as the positive control, and pure, SeO_3^{2-}-free HAp as the negative control. Se-HAp powders demonstrated a higher antibacterial activity than HAp against all four bacterial strains tested in the blood agar assay. This shows that the antibacterial effectiveness of Se-HAp is due to the presence of SeO_3^{2-} rather than HAp itself. HAp alone demonstrated a finite antibacterial activity only against *E. coli*, which was surpassed only by the post-precipitated Se-HAp containing the highest concentration of selenite (0.36 wt.%) and the co-precipitated Se-HAp containing the two highest concentrations of selenite (1.92 and 3 wt. %).

Se-HAp powders also demonstrated a significantly lower antibacterial activity than the vancomycin-loaded Se-HAp against all four types of bacteria. Although there was some increase in the zones of inhibition and in the corresponding antibacterial activity with an increase in the selenite content, e.g., against *E. coli*, this activity was often dependent on the sole presence of selenite in HAp rather than on its concentration. This suggests that the antibacterial effect on agars is mostly due to a direct surface contact between selenite on the particle surface and the bacterium rather than the release of ions or the internal structure of the particle. Se-HAp powders were most effective against *E. coli* and *S. aureus*, with the greatest effect seen in *E. coli.* For *S. enteritidis,* the inhibition was seen at higher weight contents of selenite, most pronouncedly at 1.92 wt.%. At this concentration of selenite, the inhibition of *S. enteritidis* was similar to that seen around the vancomycin-loaded Se-HAp control.

The antibacterial activity was higher for the co-precipitated powders than for the post-precipitated ones. Even though the concentration of selenite on the particle surface may be the same for co-precipitated and post-precipitated powders, the turnover of the highly mobile surface of HAp ensures that the co-precipitated powders provide for a steadier selenite surface content over time. The post-precipitated powders showed little to no antibacterial activity, with only the 0.36 wt.% Se-HAp powder being active against *E. coli* and comparable in effect to the 0.1 wt.% co-precipitated Se-HAp. Neither the vancomycin-loaded Se-HAp nor any other powders were considerably effective against the gram-negative, biofilm-forming *P. aeruginosa*. In contrast, the addition of vancomycin to the powders increased their effect against both the gram-positive, biofilm-forming *S. aureus* and the non-biofilm-forming, gram-negative *E. coli* and *S. enteritidis*.

Liquid inoculation assays corroborated the higher antibacterial activity of Se-HAp against *E. coli* than against *S. aureus*. Previously, we have shown that HAp in general has a greater antibacterial activity against the gram-negative bacteria, e.g. *E. coli*, than against the gram-positive ones, e.g. *S. aureus*[68]. Here, in liquid inoculations containing Se-HAp powders with the two highest SeO_3^{2-} weight contents, 1.92 and 3 wt.%, the number of *E. coli* colony forming units (CFU) was significantly lower than in broths containing either HAp powders with no selenite (5 – 7 times at days 2 – 3) or untreated control (4.5 - 5.5 times at days 2 – 3) throughout the duration of the assay, i.e. up to 72 h (Fig.10a). In contrast, the activity of Se-HAp powders against *S. aureus* was less consistently extended in time than that against *E. coli*, albeit present for certain Se-HAp compositions even after 72 h of the treatment when compared against selenite-free HAp (Fig.10b). The antibacterial activity of Se-HAp against *S. aureus* was most pronounced 24 hours after the inoculation of the Se-HAp-treated culture and by 48 hours the bacterial population had largely recovered to the untreated control levels, suggesting that the *S. aureus* that survived the initial Se-HAp treatment was no longer susceptible to selenite, regardless of its concentration in Se-HAp (Fig.10b). In contrast, *E. coli* remained susceptible to selenite at the highest concentrations, even by 72 hours post-treatment (Fig.10a).

3.2.2. Anticancer activity of Se-HAp—Viability of K7M2 mouse osteosarcoma cells decreased in direct proportion with the amount of selenite in HAp and was significantly different from the untreated control and from pure HAp at selenite contents equal to or higher than 1.9 wt.% (Fig.11). Pure HAp, interestingly, increased the cell viability to 130 % of the negative control, while Se-HAp richest in the selenite content, the 3 wt.% Se-HAp, reduced the viability of osteosarcoma cells by 50 % compared to pure HAp and by 60 % compared to the untreated control. In contrast, the viability of primary fibroblasts treated with either pure HAp or HAp incorporating different amounts of SeO_3^{2-} ions was not reduced (Fig.11). The viability curve as a function of the SeO_3^{2-} content in Se-HAp dipped at lower SeO_3^{2-} contents, but then recovered as the latter increased to 3 wt.%. This result shows that Se-Hap has selective toxicity for transformed cancer cells, while not affecting the viability of noncancerous primary cells. A similar selective anticancer activity *in vitro* was previously ascribed to HAp alone. For example, HAp nanoparticles added at 200 μg/ml exhibited size-dependent apoptotic effects on HepG2 hepatoma cells, but caused no toxicity

in normal, L-02 human hepatocytes[69]. They also had toxic effects on MG63 osteosarcoma cells, but left regular osteoblasts intact[70].

To assess the cell/particle interaction, the interface between Se-HAp and both K7M2 osteosarcoma cells and primary lung fibroblasts was analyzed through the use of immunofluorescent staining (Fig.12). Co-precipitated and annealed HAp powder containing 1.24 wt.% selenite was chosen for the analysis since the treatment with 1.24 wt.% Se-HAp did not cause significant cell death in either osteosarcoma cells or primary fibroblasts (Fig. 11). Examination of the cell/particle interface showed that the uptake of Se-HAp particles by either cell type does not appear to affect the morphology of the cell, disrupt the actin cytoskeleton or cause any noticeable nuclear damage. Both cell types responded in a similar manner when treated with either Se-HAp or HAp. Since the morphological effects of selenite-to-phosphate substitution are notable at this selenite content (1.24 wt.%, Fig.3), this indirectly demonstrates that the detrimental effects of Se-HAp on cancer cells are, dose-dependently, due to the presence of SeO_3^{2-} ions in HAp. Selenite was previously shown to induce apoptotic hepatocyte death via oxidative damage and the corresponding induction of the imbalance of intracellular glutathione redox cycle in a dose-dependent manner[71]. The mechanism by which selenite destroyed human bladder cancer cells is complex and consisted of a combination of mitochondrial and DNA damage, leading to death via apoptosis, necrosis and autophagy runaway typified by vacuolar shrinkage and loss of adherence[72]. Cell death mechanisms caused by selenite ions are, therefore, variable and highly dose- and cell-dependent.

3.2.3. Osteoinductive activity of Se-HAp—To determine if Se-HAp has an osteoinductive effect on osteoblast-like cells, quantification of the expression of bone gamma-carboxylglutamate (BGLAP3), an osteocalcin-related protein, was carried out on semi-differentiated MC3T3-E1 cells treated with Se-HAp powders containing different amounts of selenite ion. To that end, MC3T3-E1 cells pretreated with DMEM supplemented with ascorbic acid for 17 days were treated with Se-HAp in which the selenite weight content ranged from 0.1 - 3 wt.%. The absolute BGLAP3 expression increased in direct proportion with the amount of SeO_3^{2-} in Se-HAp and was higher than in the control, untreated cells or cells treated with selenite-free HAp particles (Fig.13a). Relative to the expression of β-actin as a housekeeping gene, BGLAP3 expression demonstrated the same trend: as selenite concentration in Se-HAp increased, from 0.1 to 1.92 wt.%, a corresponding increase in BGLAP3 expression was seen, with the highest expression detected in cells treated with 1.23 wt.% Se-HAp (Fig.13c). Cells treated with 3 wt.% Se-HAp displayed a significantly reduced expression of BGLAP3 compared to the untreated control and to the osteoblastic cells treated with Se-free HAp (Fig.13c). However, the cells treated with 3 wt.% Se-HAp were also morphologically abnormal and showed signs of cell death by 24 hours. Interestingly, the administration of Se-HAp to semi-differentiated MC3T3-E1 cells promoted the expression of GAPDH in direct proportion with the selenite concentration in Se-HAp, exhibiting a trend similar to that observed for BGLAP3 (Fig.13b). While normally thought of as a housekeeping gene that plays a role in energy metabolism, in recent years GAPDH has been found to be involved in regulating other cell functions, including cell proliferation, tumorigenesis and apoptosis[73]. The highest expression of

GAPDH was seen in cells treated with HAp containing 1.92 wt.% of selenite, which is the same concentration of selenite at which the viability of K7M2 cells was reduced by 50% (Fig.11), suggesting that the addition of Se-HAp activates signaling pathways involved in cell death, which in turn affect the expression of GAPDH in the cell. Finally, following the treatment with Se-HAp containing the largest amount of selenite, i.e. 3 wt.%, the cell death becomes pervasive and a sudden drop in the GAPDH expression is registered (Fig.13b). It is worth noting that the gene expression assays were carried out on MC3T3-E1 cells semi-differentiated for 17 days because Se-HAp, regardless of the weight content of SeO_3^{2-}, had an invariably lethal effect on undifferentiated, pre-osteoblastic MC3T3-E1 cells at the tested dose of 2 mg ml-1.

GAPDH expression is known to be elevated in stressed cells, the reason for which this gene has been proposed as an intracellular sensor of oxidative stress during early apoptosis[74]. This upregulation of GAPDH (Fig.13b) indicates that the osteoinductive effect of Se-HAp is due to an overall higher metabolic activity of cells treated with these particles. It was previously observed that the imposition of mechanochemical stress on osteoblastic MC3T3-E1 cells can have an augmentative effect on the expression of osteogenic markers[75]. Although it can have a protective, antioxidative effect on cells under attack of different species[76], selenite is an oxygen specie that itself can exert an oxidative stress on the cells[77,78] and such form of stress has been shown to be capable of leading to increased bone production in osteoblastic cells[79]. Mitochondria are tightly related to oxidative stress, which is essential to their function in spite of leading to permanent cell damage and/or cell death if excessive[80]. Also, a number of pro-inflammatory molecular mediators act as components of regeneration pathways within the cell[81], suggesting that the activation of pro-inflammatory cytokines can be a stimulus for new bone growth. It is possible that SeO_3^{2-} ions impose a concordant effect on the cells: they may induce stress to levels that boost the cell metabolism and activate the osteogenic pathways within the cell. At higher concentrations of selenite, however, e.g. 3 wt.%, the oxidative stress overwhelms the cell and causes it to activate the apoptotic pathways, with the cell death becoming the predominant outcome. This effect was observed in mineral formation too: although selenite promoted mineral formation at low contents in Se-HAp, it simultaneously exerted detrimental effects on cell morphology and viability, which resulted in no mineral formation at higher weight contents of selenite (Fig. 13d). In a bigger picture, such a promotion of beneficial effects through stress imposition agrees with the recently observed decrease in the health span, but increase in longevity as the result of selenium deficiency in diet[82]. Finally, in view of the different effects Se-HAp had on three different cell lines and four different bacterial species utilized in this study, we could conclude that the effect of Se-HAp is intensely cell- and bacterium-dependent. Such varying effects of SeO_3^{2-} ions depending on the cell line and bacterial species were documented before[83,84].

4. Conclusion

The exceptional lattice strain tolerance and charge compensation capacity of HAp crystal lattice endows it with the potential to accommodate a plethora of foreign ions, ranging from as light as lithium[85] to as heavy as uranium[86] and including both cations and anions. This ability of HAp, along with its sparsely soluble nature, makes it possible to act as a mineral

reservoir of the body and can be harnessed for various therapeutic effects through incorporation of specific and functional ions. In this study, we have shown that selenite, an anion almost identical in size to the phosphate ion, can improve the properties of pure HAp in a threefold manner: anticancer, antibacterial and osteoinductive. The incorporation of selenite into HAp increased its antibacterial activity against *E. coli* and endowed it with activity against *S. enteritidis* and *S. aureus*. Unlike the zones of inhibition, the bacterial concentrations in broths decreased in direct proportion with the content of selenite in HAp. As a corollary of its antibacterial activity, selenite was verified as a stress-imposing anion in bone cells. However, this imposition of stress, particularly noticeable at the weight content of selenite > 2 wt.%, led to an increased expression of an osteocalcin precursor, BGLAP3, in the cells, thus indicating the ability of HAp to promote a higher rate of new bone formation following the partial phosphate-to-selenite substitution. HAp powders containing the two highest concentrations of selenite ions also had pronounced inhibitory effects on the osteosarcoma cell line, while leaving the regular fibroblasts intact. Changes in the particle morphology and crystallinity following the incorporation of selenite were also documented. More sophisticated synthesis methods coupled to more detailed structural refinement studies should be the next step in the harnessing of the therapeutic effects of selenite delivered using HAp as the carrier. These and similar findings are expected to better our understanding of the effects of the natural compositional variability of bone on its properties[87] and increase our capacity to utilize this understanding for various therapeutic ends.

Acknowledgements

NIH grant R00-DE021416 is acknowledged for support. The authors thank Jarrett Mickens of the Uskokovic Lab at University of Illinois at Chicago (UIC) for running the MTT assay. This work made use of instruments in the Electron Microscopy Service (Research Resources Center, UIC).

References

1. Supova M. Problem of hydroxyapatite dispersion in polymer matrices: a review. J Mater Sci Mater Med. 2009; 20(6):1201–13. [PubMed: 19225871]
2. Dorozhkin SV. Self-setting calcium orthophosphate formulations. J. Funct Biomater. 2013; 4:209–311. [PubMed: 24956191]
3. Uskoković V, Wu VM. Calcium Phosphate as a Key Material for Socially Responsible Tissue Engineering. Materials. 2016; 9:434–460. [PubMed: 27347359]
4. Becker J, Lu L, Runge MB, Zeng H, Yaszemski MJ, Dadsetan M. Nanocomposite bone scaffolds based on biodegradable polymers and hydroxyapatite. J Biomed Mater Res A. 2015; 103:2549–57. [PubMed: 25504776]
5. Allori AC, Sailon AM, Warren SM. Biological basis of bone formation, remodeling, and repair-part II: extracellular matrix. Tissue Eng. Part B. Rev. 2008; 14:275–283. [PubMed: 19183102]
6. Uskoković V. Nanostructured Platforms for the Sustained and Local Delivery of Antibiotics in the Treatment of Osteomyelitis. Critical Reviews in Therapeutic Drug Carrier Systems. 2015; 32(1):1–59. [PubMed: 25746204]
7. Ossipov DA. Bisphosphonate-modified biomaterials for drug delivery and bone tissue engineering. Expert Opin. Drug Deliv. 2015; 12:1443–58. [PubMed: 25739860]
8. Uskoković V, Desai TA. In vitro analysis of nanoparticulate hydroxyapatite/chitosan composites as potential drug delivery platforms for the sustained release of antibiotics in the treatment of osteomyelitis. J. Pharm. Sci. 2014; 103:567–579. [PubMed: 24382825]

9. Uskoković V, Desai TA. Simultaneous bactericidal and osteogenic effect of nanoparticulate calcium phosphate powders loaded with clindamycin on osteoblasts infected with Staphylococcus aureus. Mater. Sci. Eng. C. Mater. Biol. Appl. 2014; 37:210–22. [PubMed: 24582242]
10. Yang H, Hao L, Zhao N, Du C, Wang Y. Hierarchical porous hydroxyapatite microsphere as drug delivery carrier. CrystEngComm. 2013; 15(29):5760.
11. Tampieri A, D'Alessandro T, Sandri M, Sprio S, Landi E, Bertinetti L, Panseri S, Pepponi G, Goettlicher J, Bañobre-López M, Rivas J. Intrinsic magnetism and hyperthermia in bioactive Fe-doped hydroxyapatite. Acta Biomater. 2012; 8(2):843–851. [PubMed: 22005331]
12. Rodríguez-Ruiz I, Delgado-López JM, Durán-Olivencia MA, Iafisco M, Tampieri A, Colangelo D, Prat M, Gómez-Morales J. pH-Responsive Delivery of Doxorubicin from Citrate–Apatite Nanocrystals with Tailored Carbonate Content. Langmuir. 2013; 29(26):8213–8221. [PubMed: 23735159]
13. Wopenka B, Pasteris JD. A mineralogical perspective on the apatite in bone. Mater. Sci. Eng. C. 2005; 25(2):131–143.
14. Yajing Y, Qiongqiong D, Yong H, Han S, Pang X. Magnesium substituted hydroxyapatite coating on titanium with nanotubular TiO_2 intermediate layer via electrochemical deposition. Appl. Surf. Sci. 2014; 305:77–85.
15. Landi E, Logroscino G, Proietti L, Tampieri A, Sandri M, Sprio S. Biomimetic Mg-substituted hydroxyapatite: from synthesis to in vivo behaviour. J. Mater. Sci. Mater. Med. 2008; 19(1):239–247. [PubMed: 17597369]
16. Martínez-Casado FJ, Iafisco M, Delgado-López JM, Martínez-Benito C, Ruiz-Pérez C, Colangelo D, Oltolina F, Prat M, Gómez-Morales J. Bioinspired Citrate–Apatite Nanocrystals Doped with Divalent Transition Metal Ions. Cryst. Growth Des. 2016; 16(1):145–153.
17. Boanini E, Gazzano M, Bigi A. Ionic substitutions in calcium phosphates synthesized at low temperature. Acta Biomater. 2010; 6:1882–1894. [PubMed: 20040384]
18. Kaygili O, Dorozhkin SV, Ates T, Al-Ghamdi A. a. Yakuphanoglu F. Dielectric properties of Fe doped hydroxyapatite prepared by sol-gel method. Ceram. Int. 2014; 40(7):9395–9402.
19. Gloria A, Russo T, D'Amora U, Zeppetelli S, D'Alessandro T, Sandri M, Bañobre-López M, Piñeiro-Redondo Y, Uhlarz M, Tampieri a, Rivas J, Herrmannsdörfer T, Dediu V. a, Ambrosio L, De Santis R. Magnetic poly(ε-caprolactone)/iron-doped hydroxyapatite nanocomposite substrates for advanced bone tissue engineering. J. R. Soc. Interface. 2013; 10(80):20120833. [PubMed: 23303218]
20. Jiang H, Li Y, Zuo Y, Yang W, Zhang L, Li J, Wang L, Zou Q, Cheng L, Li J. Physical and Chemical Properties of Superparamagnetic Fe-Incorporated Nano Hydroxyapatite. J Nanosci Nanotechnol. 2009; 9:6844–50. [PubMed: 19908688]
21. Nakahira A, Nakamura S, Horimoto M. Synthesis of modified hydroxyapatite (HAP) substituted with Fe ion for DDS application. IEEE Trans. Magn. 2007; 43(6):2465–2467.
22. Panseri S, Cunha C, D'Alessandro T, Sandri M, Giavaresi G, Marcacci M, Hung CT, Tampieri A. Intrinsically superparamagnetic Fe-hydroxyapatite nanoparticles positively influence osteoblast-like cell behaviour. J. Nanobiotechnology. 2012; 10(1):32. [PubMed: 22828388]
23. Ignjatović N, Ajduković Z, Savić V, Najman S, Mihailović D, Vasiljević P, Stojanović Z, Uskoković V, Uskoković D. Nanoparticles of cobalt-substituted hydroxyapatite in regeneration of mandibular osteoporotic bones. J. Mater. Sci. Mater. Med. 2013; 24(2):343–354. [PubMed: 23090835]
24. Tank KP, Chudasama KS, Thaker VS, Joshi MJ. Cobalt-doped nanohydroxyapatite: Synthesis, characterization, antimicrobial and hemolytic studies. J. Nanoparticle Res. 2013; 15(5):474–479.
25. Patel N, Best SM, Bonfield W, Gibson IR, Hing K. a. Damien E, Revell P. a. A comparative study on the in vivo behavior of hydroxyapatite and silicon substituted hydroxyapatite granules. J. Mater. Sci. Mater. Med. 2002; 13(12):1199–206. [PubMed: 15348666]
26. Lim PN, Chang L, Thian ES. Development of nanosized silver-substituted apatite for biomedical applications: A review. Nanomedicine. 2015; 11:1331–1344. [PubMed: 25943400]
27. Lin YG, Yang ZR, Jiang C. Preparation, characterization and antibacterial property of cerium substituted hydroxyapatite nanoparticles. J Rare Earths. 2007; 25:452–456.

28. Iconaru SL, Motelia-Heino M, Predoi D. Study on europium-doped hydroxyapatite nanoparticles by Fourier Transform Infrared Spectroscopy and Their Antimicrobial Properties. J Spectroscopy. 2013 Article ID 284285.
29. Landi E, Tampieri A, Celotti G, Sprio S, Sandri M, Logroscino G. Sr-substituted hydroxyapatites for osteoporotic bone replacement. Acta Biomater. 2007; 3(6):961–969. [PubMed: 17618844]
30. Landi E, Celotti G, Logroscino G, Tampieri A. Carbonated hydroxyapatite as bone substitute. J. Eur. Ceram. Soc. 2003; 23(15):2931–2937.
31. Chen M-H, Hanagata N, Ikoma T, Huang J-Y, Li K-Y, Lin C-P, Lin F-H. Hafnium-doped hydroxyapatite nanoparticles with ionizing radiation for lung cancer treatment. Acta Biomaterialia. 2016; 37:165–73. [PubMed: 27060620]
32. Badmaev V, Majeed M, Passwater RA. Selenium: a quest for better understanding. Altern. Ther. Health Med. 1996; 2(4):59–62. 65–7.
33. Ralston NV, Raymond LJ. Dietary selenium's protective effects against methylmercury toxicity. Toxicology. 2010; 278:112–23. [PubMed: 20561558]
34. Tran PL, Hammond AA, Mosley T, Cortez J, Gray T, Colmer-Hamood JA, Shashtri M, Spallholz JE, Hamood AN, Reid TW. Organoselenium coating on cellulose inhibits the formation of biofilms by Pseudomonas aeruginosa and Staphylococcus aureus. Appl. Environ. Microbiol. 2009; 75(11): 3586–3592. [PubMed: 19346348]
35. Drake EN. Cancer chemoprevention: selenium as a prooxidant, not an antioxidant. Med. Hypotheses. 2006; 67(2):318–322. [PubMed: 16574336]
36. Moreno-Reyes R, Egrise D, Neve J, Pasteels JL, Schoutens A. Selenium deficiency-induced growth retardation is associated with an impaired bone metabolism and osteopenia. J. Bone Miner. Res. 2001; 16(8):1556–1563. [PubMed: 11499879]
37. Vekariya KK, Kaur J, Tikoo L. Alleviating anastrazole induced bone toxicity by selenium nanoparticles in SD rats. Toxicol Appl Pharmacol. 2013; 268:212–220. [PubMed: 23415680]
38. Turan B, Can B, Delilbasi E. Selenium combined with vitamin E and vitamin C restores structural alterations of bones in heparin-induced osteoporosis. Clin Rheumatol. 2003; 22:432–436. [PubMed: 14677021]
39. Uskokovic V. The Role of Hydroxyl Channel in Defining Selected Physicochemical Peculiarities Exhibited by Hydroxyapatite. RSC Adv. 2015; 5(46):36614–36633. [PubMed: 26229593]
40. Kolmas J, Kuras M, Oledzka E, Sobczak M. A solid-state NMR study of selenium substitution into nanocrystalline hydroxyapatite. Int J Mol Sci. 2015; 16:11452–64. [PubMed: 25997001]
41. Kolmas J, Oledzka E, Sobczak M, Nałęcz-Jawecki G. Nanocrystalline hydroxyapatite doped with selenium oxyanions: A new material for potential biomedical applications. Mater. Sci. Eng. C. 2014; 39:134–142.
42. Rodríguez-Valencia C, López-Álvarez M, Cochón-Cores B, Pereiro I, Serra J, González P. Novel selenium-doped hydroxyapatite coatings for biomedical applications. J. Biomed. Mater. Res. Part A. 2013; 101A(3):853–861.
43. Trampuz A, Widmer AF. Infections associated with orthopedic implants. Curr.Opin.Infect.Dis. 2006; 19:349–356. [PubMed: 16804382]
44. Arciola CR, Campoccia D, Speziale P, Montanaro L, Costerton JW. Biofilm formation in Staphylococcus implant infections. A review of molecular mechanisms and implications for biofilm-resistant materials. Biomaterials. 2012; 33(26):5967–5982. [PubMed: 22695065]
45. Yanhua W, Hao H, Li Y, Zhang S. Selenium-substituted hydroxyapatite nanoparticles and their in vivo antitumor effect on hepatocellular carcinoma. Colloids Surfaces B Biointerfaces. 2016; 140:297–306. [PubMed: 26764116]
46. Chen X, Cai K, Fang J, Lai M, Hou Y, Li J, Luo Z, Hu Y, Tang L. Fabrication of selenium-deposited and chitosan-coated titania nanotubes with anticancer and antibacterial properties. Colloids Surfaces B Biointerfaces. 2013; 103:149–157. [PubMed: 23201732]
47. Tran PA, Sarin L, Hurt RH, Webster TJ. Differential effects of nanoselenium doping on healthy and cancerous osteoblasts in coculture on titanium. Int. J. Nanomedicine. 2010; 5(1):351–358. [PubMed: 20517480]
48. Landi E, Tampieri A, Celotti G, Sprio S. Densification behaviour and mechanisms of synthetic hydroxyapatites. J. Eur. Ceram. Soc. 2000; 20(14–15):2377–2387.

49. Pfaffl MW. A New Mathematical Model for Relative Quantification in Real-Time RTPCR. Nucleic Acids Research. 2001; 29:e45. [PubMed: 11328886]
50. Kawasaki T, Takahashi S, Ikeda K. Hydroxyapatite high-performance liquid chromatography: column performance for proteins. European Journal of Biochemistry. 1985; 152:361–371. [PubMed: 2414102]
51. Cummings LJ, Snyder MA, Brisack K. Protein chromatography on hydroxyapatite columns. Methods Enzymol. 2009; 463:387–404. [PubMed: 19892184]
52. Mahabole MP, Aiyer RC, Ramakrishna CV, Sreedhar B, Khairnar RS. Synthesis, characterization and gas sensing property of hydroxyapatite ceramic. Bulletin of Materials Science. 2005; 28:535–545.
53. Dimitrijevic A, Velickovic D, Bihelovic F, Bezbradica D, Jankov R, Milosavic N. One-step, inexpensive high yield strategy for Candida antarctica lipase A isolation using hydroxyapatite. Bioresour. Technol. 2012; 107:358–362. [PubMed: 22209131]
54. Meski S, Ziani S, Khireddine H, Yataghane F, Ferguene N. Elaboration of the hydroxyapatite with different precursors and application for the retention of the lead. Water Sci. Technol. 2011; 63(10): 2087–2096. [PubMed: 21977625]
55. Kanno CM, Sanders RL, Flynn SM, Lessard G, Myneni SCB. Novel apatite-based sorbent for defluoridation: synthesis and sorption characteristics of nano-micro-crystalline hydroxyapatite-coated-limestone. Environ. Sci. Technol. 2014; 48(10):5798–5807. [PubMed: 24766407]
56. Duc M, Lefevre G, Fedoroff M, Jeanjean J, Rouchaud JC, Monteil-Rivera F, Dumonceau J, Milonjic S. Sorption of selenium anionic species on apatites and iron oxides from aqueous solutions. J Environ Radioact. 2003; 70:61–72. [PubMed: 12915060]
57. Mohammad M, Sadaf S, Shahid A. On the Formation of Hydroxyapatite Nano Crystals Prepared Using Cationic Surfactant. Materials Research. 2015; 18(3):468–472.
58. Liu C, Huang Y, Shen W, Cui J. Kinetics of hydroxyapatite precipitation at pH 10 to 11. Biomaterials. 2001; 22(4):301–306. [PubMed: 11205432]
59. Wang A, Liu D, Yin H, Wu H, Wada Y, Ren M, Jiang T, Cheng X, Xu Y. Size-controlled synthesis of hydroxyapatite nanorods by chemical precipitation in the presence of organic modifiers. Mater. Sci. Eng. C. 2007; 27(4):865–869.
60. Zhang W, Chai Y, Cao N, Wang Y. Synthesis and characterization of selenium substituted hydroxyapatite via a hydrothermal procedure. Mater. Lett. 2014; 134:123–125.
61. Liu Y, Ma J, Zhang S. Synthesis and thermal stability of selenium-doped hydroxyapatite with different substitutions. Front. Mater. Sci. 2015; 9(4):392–396.
62. Monteil-Rivera F, Fedoroff M, Jeanjean J, Minel L, Barthes M, Dumonceau J. Sorption of Selenite (SeO(3)(2-)) on Hydroxyapatite: An Exchange Process. J. Colloid Interface Sci. 2000; 221(2): 291–300. [PubMed: 10631033]
63. Orme, JLGCA. The Use Of Scanning Probe Microscopy To Investigate Crystal-Fluid Interfaces. In: Skowronski, CAWM., DeYoreo, JJ., editors. Perspectives on Inorganic, Organic, and Biological Crystal Growth: From Fundamentals to Applications. Melville; NY: 2007.
64. Uskoković V, Li W, Habelitz S. Biomimetic Precipitation of Uniaxially Grown Calcium Phosphate Crystals from Full-Length Human Amelogenin Sols. Journal of Bionic Engineering. 2011; 8(2): 114–121. [PubMed: 22140380]
65. Giocondi J, El-Dasher BS, Nancollas GH, Orme CA. Molecular mechanisms of crystallization impacting calcium phosphate cements. Phil. Trans. R. Soc. A. 2010; 368:1937–1961. [PubMed: 20308110]
66. Ren F, Lu X, Leng Y. Ab initio simulation on the crystal structure and elastic properties of carbonated apatite. J. Mech. Behav. Biomed. Mater. 2013; 26:59–67. [PubMed: 23811277]
67. Ma J, Wang Y, Zhou L, Zhang S. Preparation and characterization of selenite substituted hydroxyapatite. Mater. Sci. Eng. C. 2013; 33(1):440–445.
68. Ghosh S, Wu VM, Pernal S, Uskoković V. Self-Setting Calcium Phosphate Cements with Tunable Antibiotic Release Rates for Advanced Bone Graft Applications. ACS Applied Materials and Interfaces. 2016; 8(12):7691–7708. [PubMed: 26958867]

69. Yuan Y, Liu C, Qian J, Wang J, Zhang Y. Size-mediated cytotoxicity and apoptosis of hydroxyapatite nanoparticles in human hepatoma HepG2 cells. Biomaterials. 2010; 31(4):730. [PubMed: 19836072]
70. Qing F, Wang Z, Hong Y, Liu M, Guo B, Luo H, Zhang X. Selective effects of hydroxyapatite nanoparticles on osteosarcoma cells and osteoblasts. J Mater Sci Mater Med. 2012; 23:2245–2251. [PubMed: 22903597]
71. Misra S, Niyogi S. Selenite causes cytotoxicity in rainbow trout (Oncorhynchus mykiss) hepatocytes by inducing oxidative stress. Toxicol In Vitro. 2009; 23(7):1249–58. [PubMed: 19651203]
72. Rezacova K, Canova K, Bezrouk A, Rudolf E. Selenite induces DNA damage and specific mitochondrial degeneration in human bladder cancer cells. Toxicol In Vitro. 2016; 32:105–114. [PubMed: 26718266]
73. Nicholls C, Li H, Liu JP. GAPDH: a common enzyme with uncommon functions. Clin Exp Pharmacol Physiol. 2012; 39(8):674–9. [PubMed: 21895736]
74. Chuang DM, Hough C, Senatorov VV. Glyceraldehyde-3-phosphate dehydrogenase, apoptosis, and neurodegenerative diseases. Annu Rev Pharmacol Toxicol. 2005; 45:269–90. [PubMed: 15822178]
75. Uskoković V, Desai TA. Does Translational Symmetry Matter? Fibroblastic and Osteoblastic Interactions with the Topographically Distinct Poly(ε-Caprolactone)/Hydroxyapatite Thin Films. ACS Applied Materials and Interfaces. 2014; 6(15):13209–13220. [PubMed: 25014232]
76. Taskin E, Dursun N. The protection of selenium on adriamycin-induced mitochondrial damage in rat. Biol Trace Elem Res. 2012; 147(1-3):165–71. [PubMed: 22237420]
77. Qi HP, Wei SQ, Gao XC, Yu NN, Hu WZ, Bi S, Cui H. Ursodeoxycholic acid prevents selenite-induced oxidative stress and alleviates cataract formation: In vitro and in vivo studies. Mol Vis. 2012; 18:151–60. [PubMed: 22275806]
78. Rooban BN, Sasikala V, Devi VG, Sahasranamam V, Abraham A. Prevention of selenite induced oxidative stress and cataractogenesis by luteolin isolated from Vitex negundo. Chem Biol Interact. 2012; 196:30–8. [PubMed: 22342831]
79. Rajamannan NM. Oxidative-mechanical stress signals stem cell niche mediated Lrp5 osteogenesis in eNOS(−/−) null mice. J Cell Biochem. 2012; 113(5):1623–34. [PubMed: 22359381]
80. Ost M, Coleman V, Kasch J, Klaus S. Regulation of myokine expression: Role of exercise and cellular stress. Free Radic Biol Med. 2016; 98:78–89. [PubMed: 26898145]
81. Thomas MV, Puleo DA. Infection, inflammation, and bone regeneration: a paradoxical relationship. J. Dent. Res. 2011; 90:1052–61. [PubMed: 21248364]
82. Wu RT, Cao L, Mattson E, Witwer KW, Cao J, Zeng H, He X, Combs GF Jr. Cheng WH. Opposing impacts on healthspan and longevity by limiting dietary selenium in telomere dysfunctional mice. Aging Cell. 2017; 16:125–135. [PubMed: 27653523]
83. Badr DM, Hafez HF, Agha AM, Shouman SA. The Combination of α-Tocopheryl Succinate and Sodium Selenite on Breast Cancer: A Merit or a Demerit? Oxid Med Cell Longev. 2016; 2016:4741694. [PubMed: 27127548]
84. Kolmas J, Groszyk E, Piotrowska U. Nanocrystalline hydroxyapatite enriched in selenite and manganese ions: physicochemical and antibacterial properties. Nanoscale Res Lett. 2015; 10(1): 989. [PubMed: 26138453]
85. Mayer I, Berger U, Markitziu A, Gedalia I. The uptake of lithium ions by synthetic carbonated hydroxyapatite. Calcif. Tissue Int. 1986; 38:293–295. [PubMed: 3087603]
86. Chatelain G, Bourgeois D, Ravaux J, Averseng O, Vidaud C, Meyer D. Incorporation of uranium into a biomimetic apatite: physicochemical and biological aspects. J. Biol. Inorg. Chem. 2015; 20:497–507. [PubMed: 25534663]
87. Pasteris JD, Wopenka B, Valsami-Jones E. Bone and Tooth Mineralization: Why Apatite? Elements. 2008; 4:97–104.

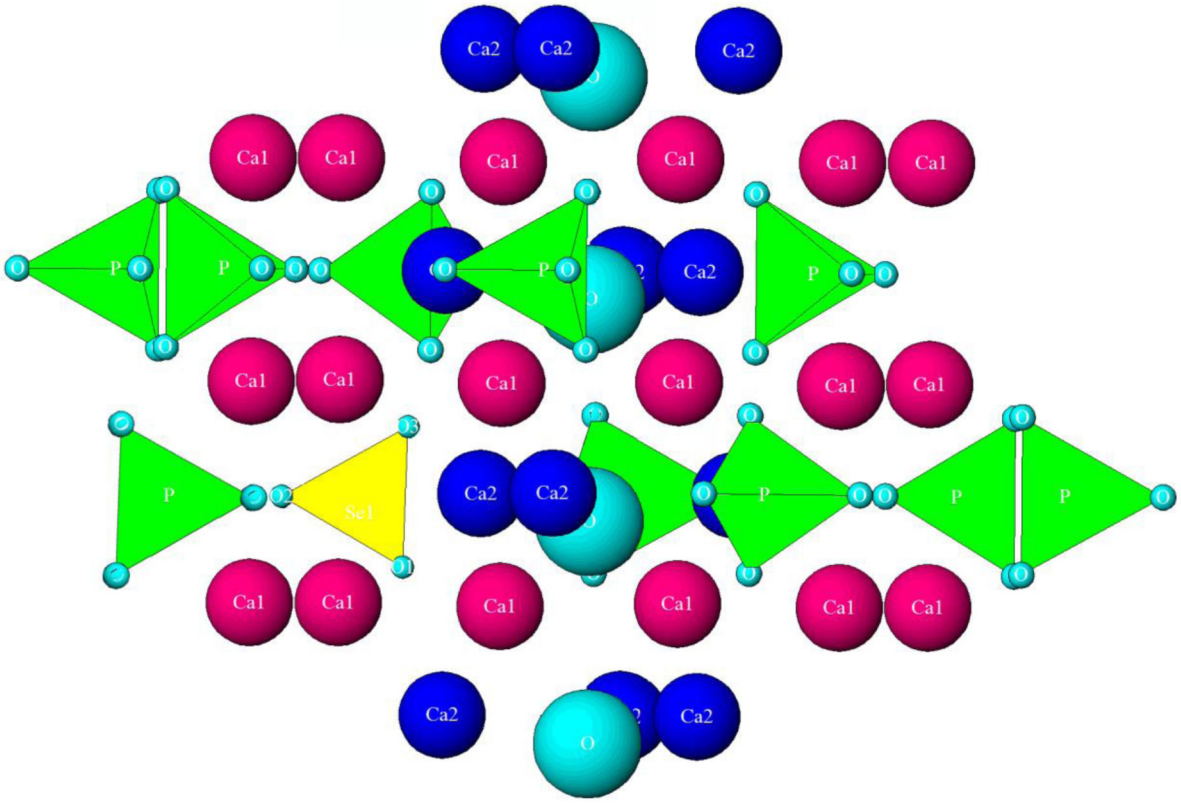

Fig.1.

Hexagonal crystal structure of HAp (space group $P6_3/m$) in which a trigonal selenite pyramid (yellow) has substituted one of six phosphate tetrahedra (green) accommodated inside a single unit cell of HAp. Columnar, Ca1 ions are shown in magenta and the hexagonal, Ca2 ions are shown in blue, while channel hydroxyl groups are depicted in turquoise.

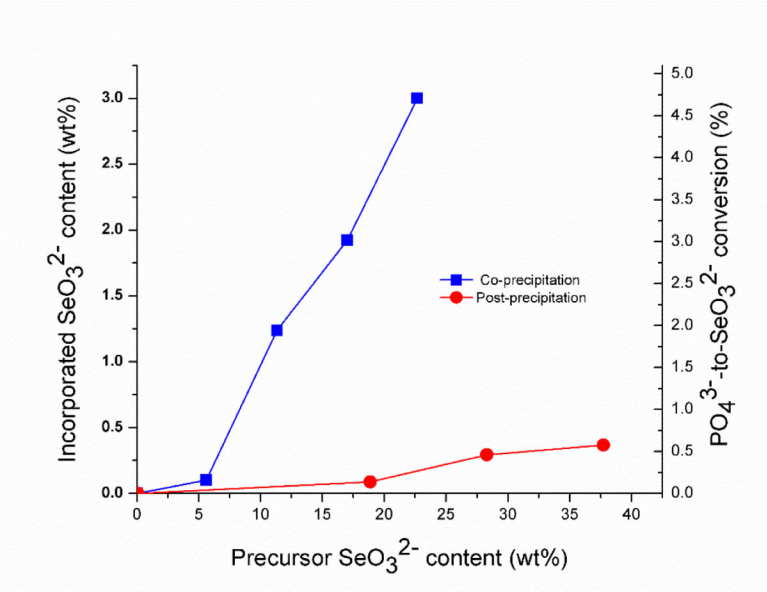

Fig.2.

Selenite content of the co-precipitated and post-precipitated Se-HAp powders and the phosphate-to-selenite conversion ratio as a function of the weight proportion of selenite ions in the synthesis solution.

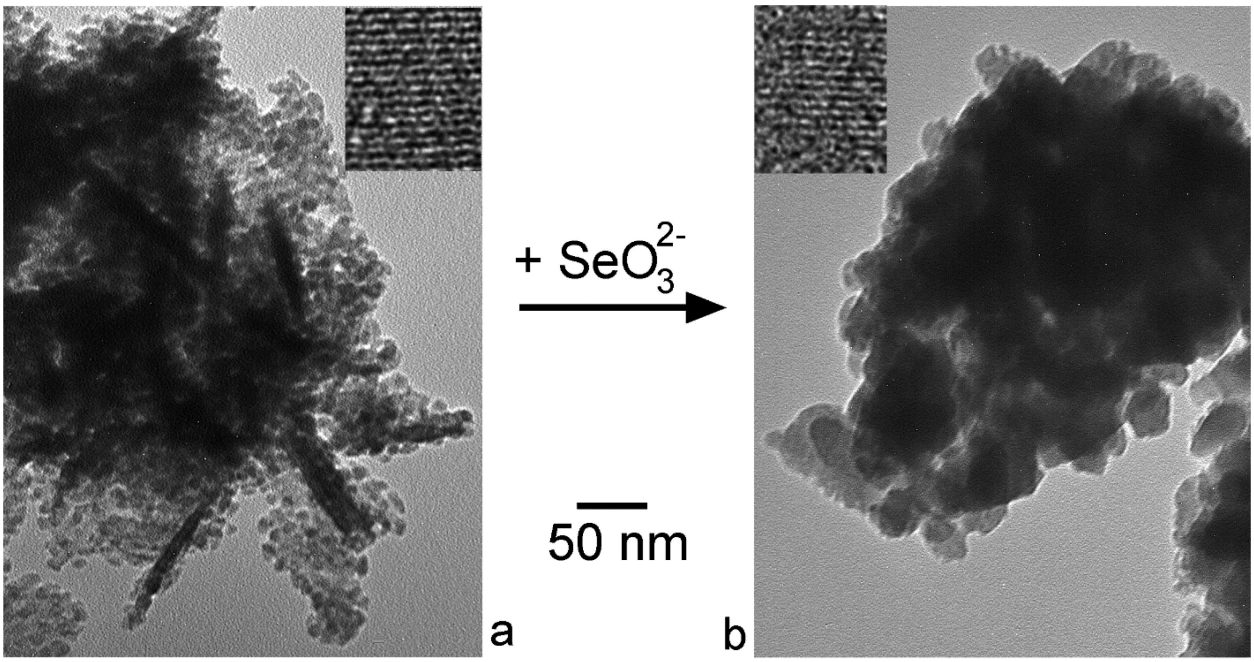

Fig.3.

Transmission electron micrographs of annealed co-precipitated HAp (a) and Se-HAp containing 1.2 wt.% of selenite (b).

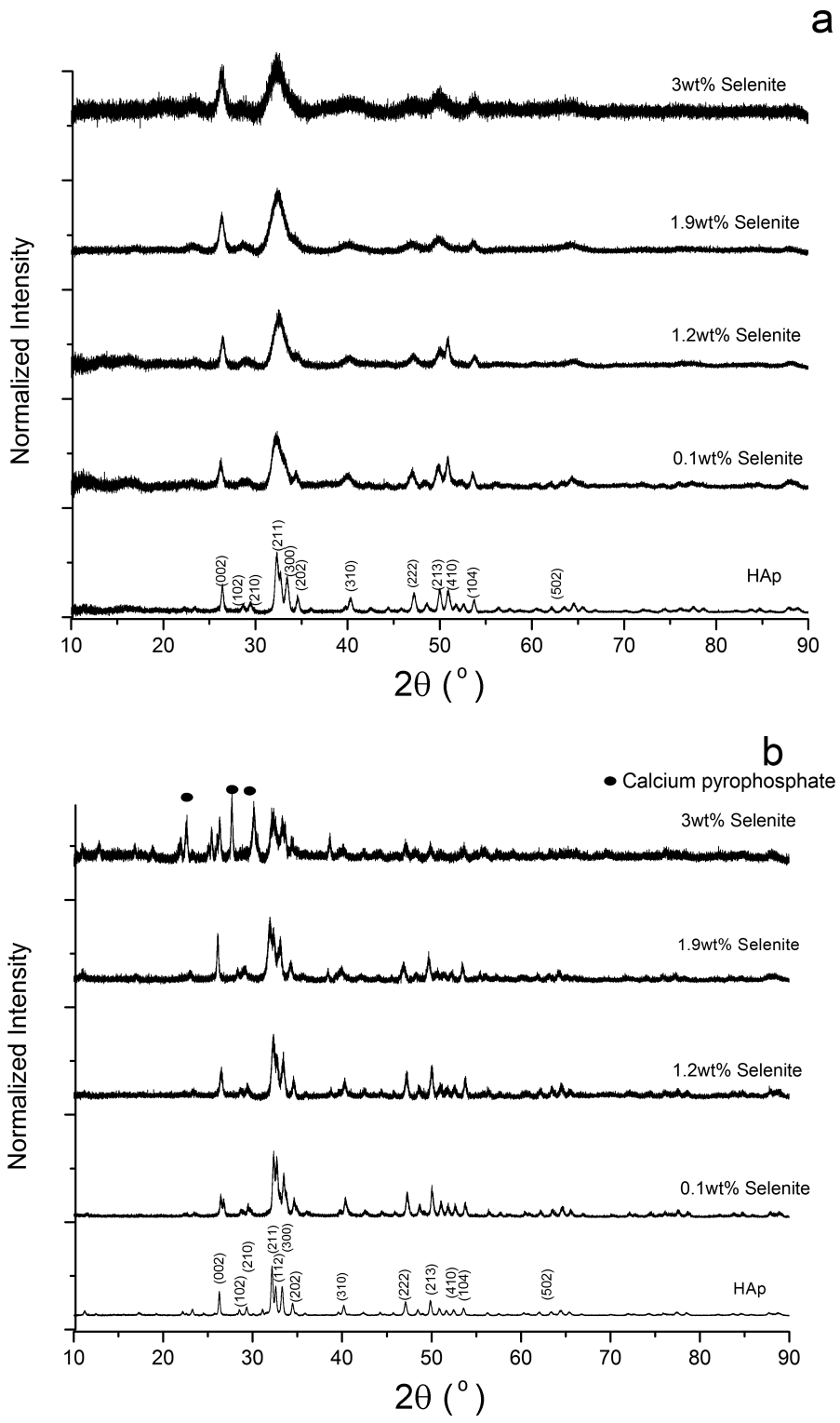

Fig.4.

X-ray diffractograms of (a) as-precipitated and (b) annealed HAp powders containing different weight percentages of selenite and synthesized by the co-precipitation method. Reflections originating from HAp are labeled with their corresponding Miller indices,

whereas reflections originating from calcium pyrophosphate (β-$Ca_2P_2O_7$) are labeled with ●.

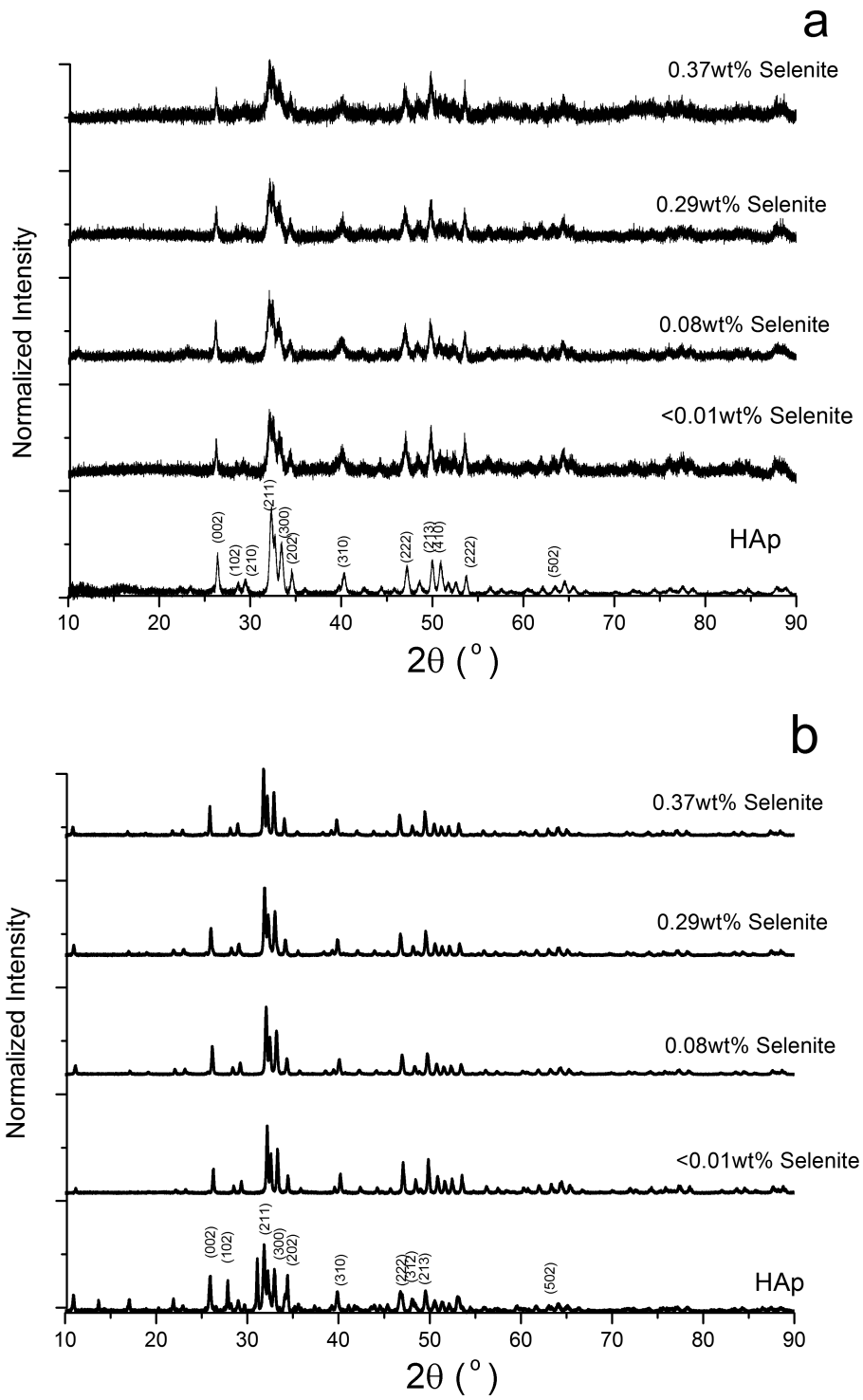

Fig.5.

X-ray diffractograms of (a) as-precipitated and (b) annealed HAp powders containing different weight percentages of selenite and synthesized by the post-precipitation method. Reflections originating from HAp are labeled with their corresponding Miller indices.

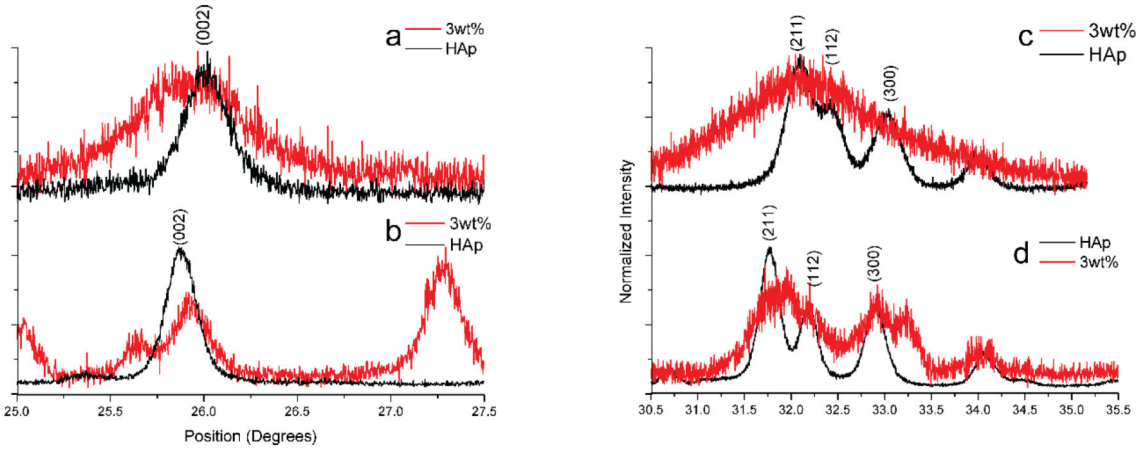

Fig.6.

A change in the (002) and (300) diffraction peaks of HAp following the incorporation of 3 wt.% of selenite by co-precipitation before (a, c) and after (b, d) annealing.

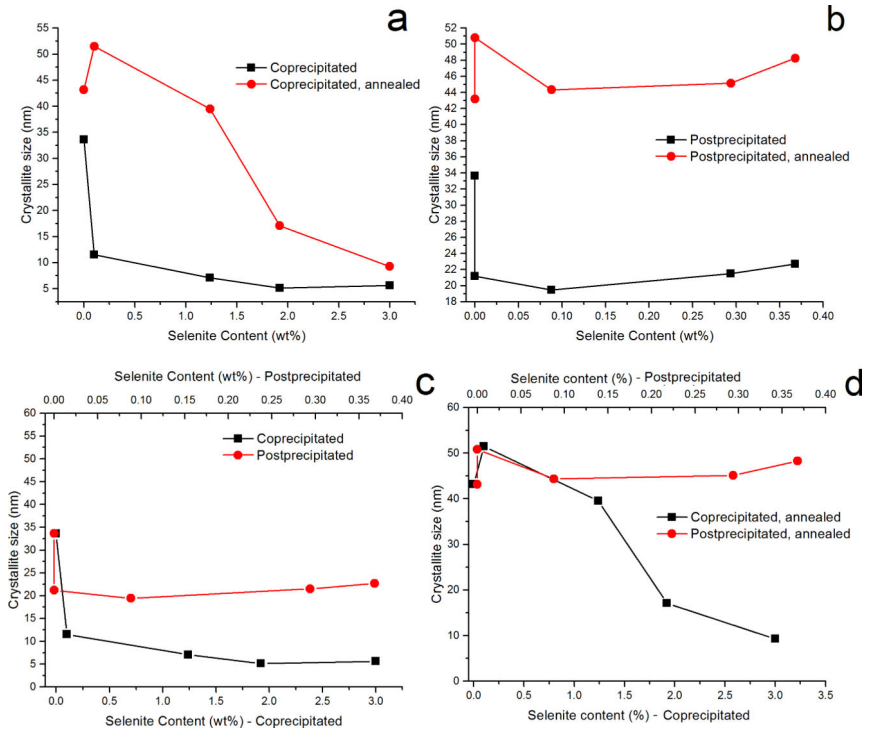

Fig.7.

Crystallite size as a function of selenite content for the following HAp powders: (a) co-precipitated powders before (-■-) and after (-●-) annealing; (b) post-precipitated powders before (-■-) and after (-●-) annealing; (c) as-precipitated powders prepared by co-precipitation (-■-) and post-precipitation (-●-); (d) annealed powders prepared by co-precipitation (-■-) and post-precipitation (-●-).

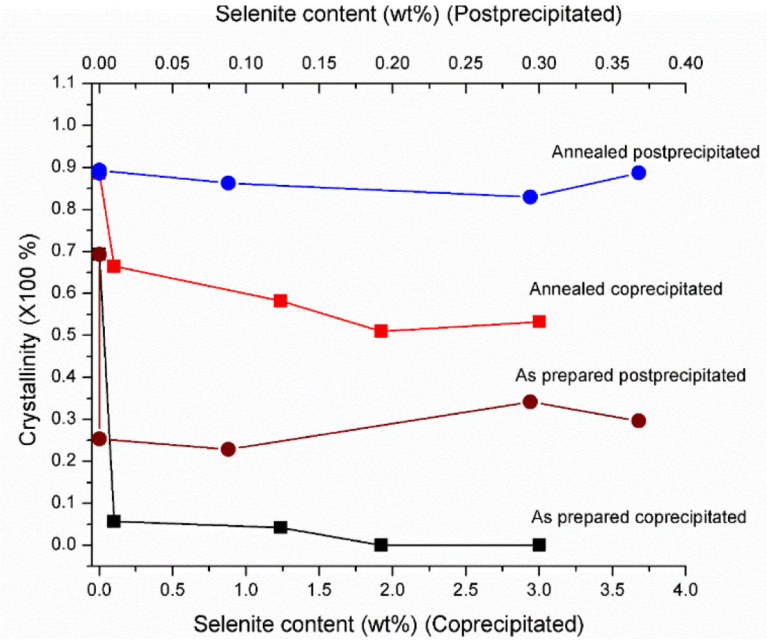

Fig.8.

Crystallinity as a function of selenite content for the following HAp powders: co-precipitated powders before (-■-) and after (-■-) annealing; post-precipitated powders before (-●-) and after (-●-) annealing.

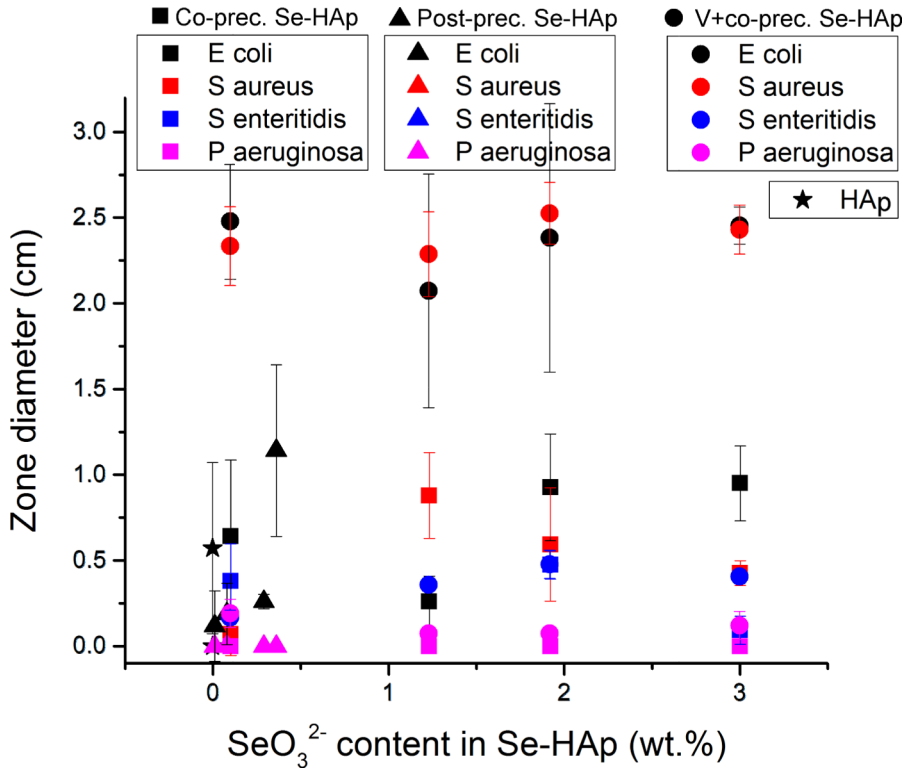

Fig.9.

Diameters of inhibition zones around annealed co-precipitated and post-precipitated Se-HAp with different contents of selenite in the agar diffusion test against *E. coli, S. aureus, S. enteritidis,* and *P. aeruginosa*. Co-precipitated Se-HAp powders loaded with vancomycin (V + co-prec. Se-HAp) and HAp particles with no selenite and no added antibiotic (HAp) were used as positive and negative controls, respectively. Blue and red triangles are invisible because of the overlap with purple triangles at 0 cm zone diameters. Blue squares are invisible at 0.48 cm for 1.92 wt.% co-precipitated Se-HAp and at 0.1 cm for 3 wt.% co-precipitated Se-HAp because of the overlap with a blue circle and a pink square, respectively.

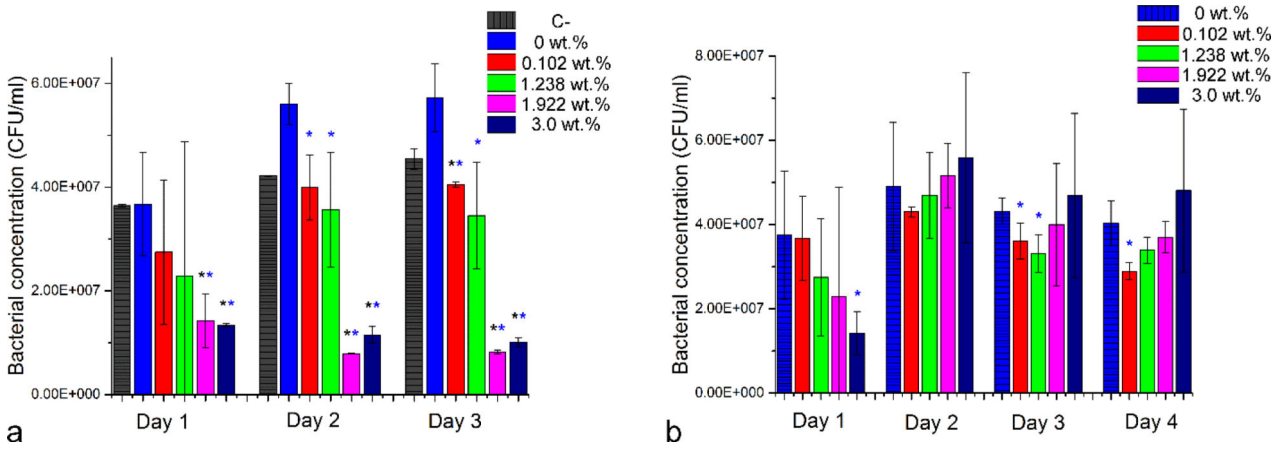

Fig.10.

Concentrations of *E. coli* (a) and *S. aureus* (b) in a liquid broth inoculation assay of co-precipitated and annealed Se-HAp powders containing different amounts of selenite and no added antibiotics. Assays were run after different incubation times, ranging from 1 to 4 days. Data are shown as averages with error bars representing standard deviation. Data points significantly lower than the untreated control (C-, $p < 0.05$) are topped with a black asterisk. Data points significantly lower than Se-free HAp (0 wt.%, $p < 0.05$) are topped with a blue asterisk.

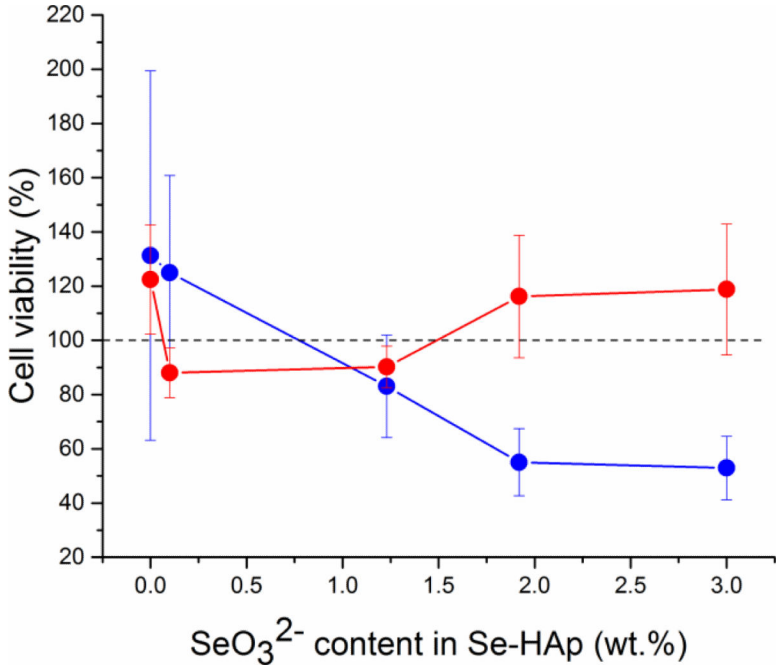

Fig.11.

Cell viability of K7M2 mouse osteosarcoma cells (-●-) and primary fibroblasts (-■-) exposed to annealed Se-HAp with various weight contents of selenite synthesized by co-precipitation. The dashed line at 100 % viability denotes the viability of untreated cells, to which the viabilities of cells treated with HAp and Se-HAp were normalized.

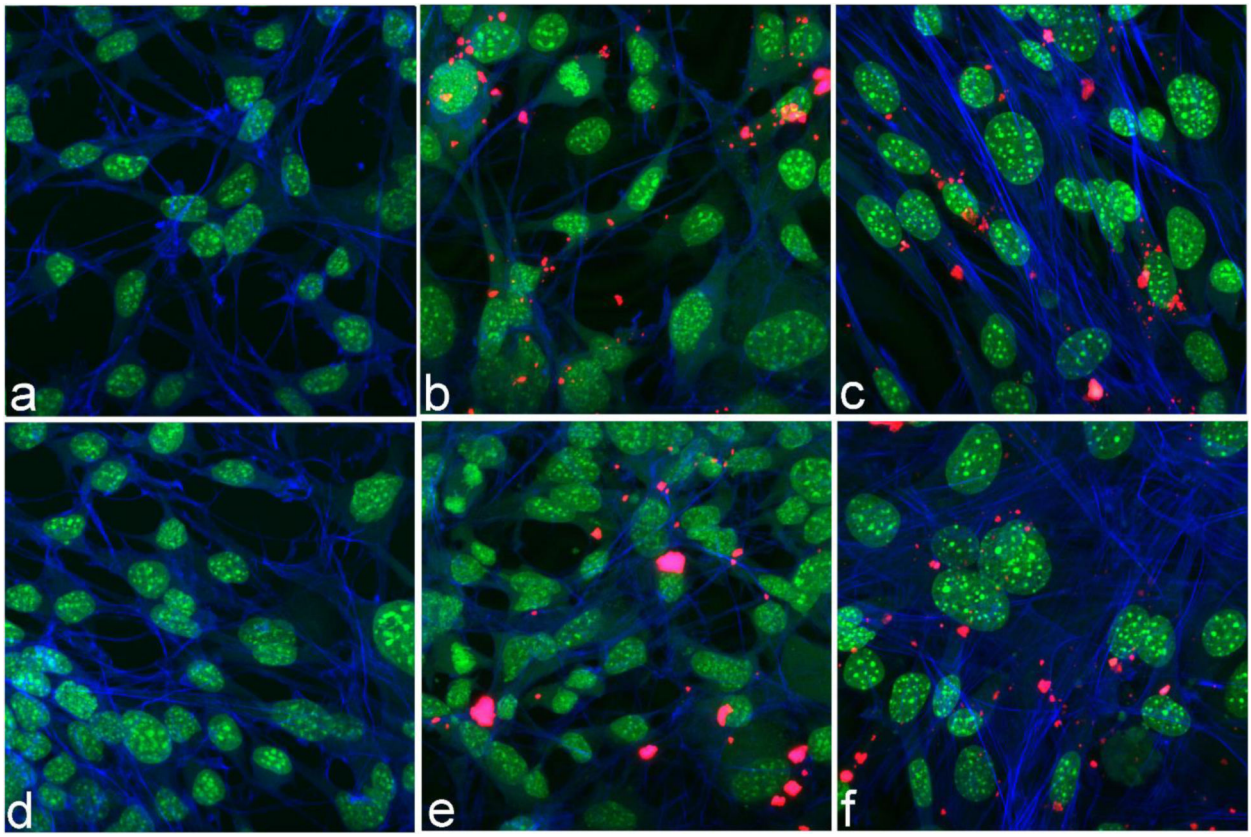

Fig.12.

Immunofluorescent optical images of primary lung fibroblasts (a-c) and K7M2 osteosarcoma cells (d-f) following a 24 h interaction with either no particles (a, d) or HAp (b, e) and Se-HAp (c, f) particles containing 1.24 wt.% selenite. Cell nucleus is stained in green, f-actin in blue, and HAp/Se-HAp particles in red.

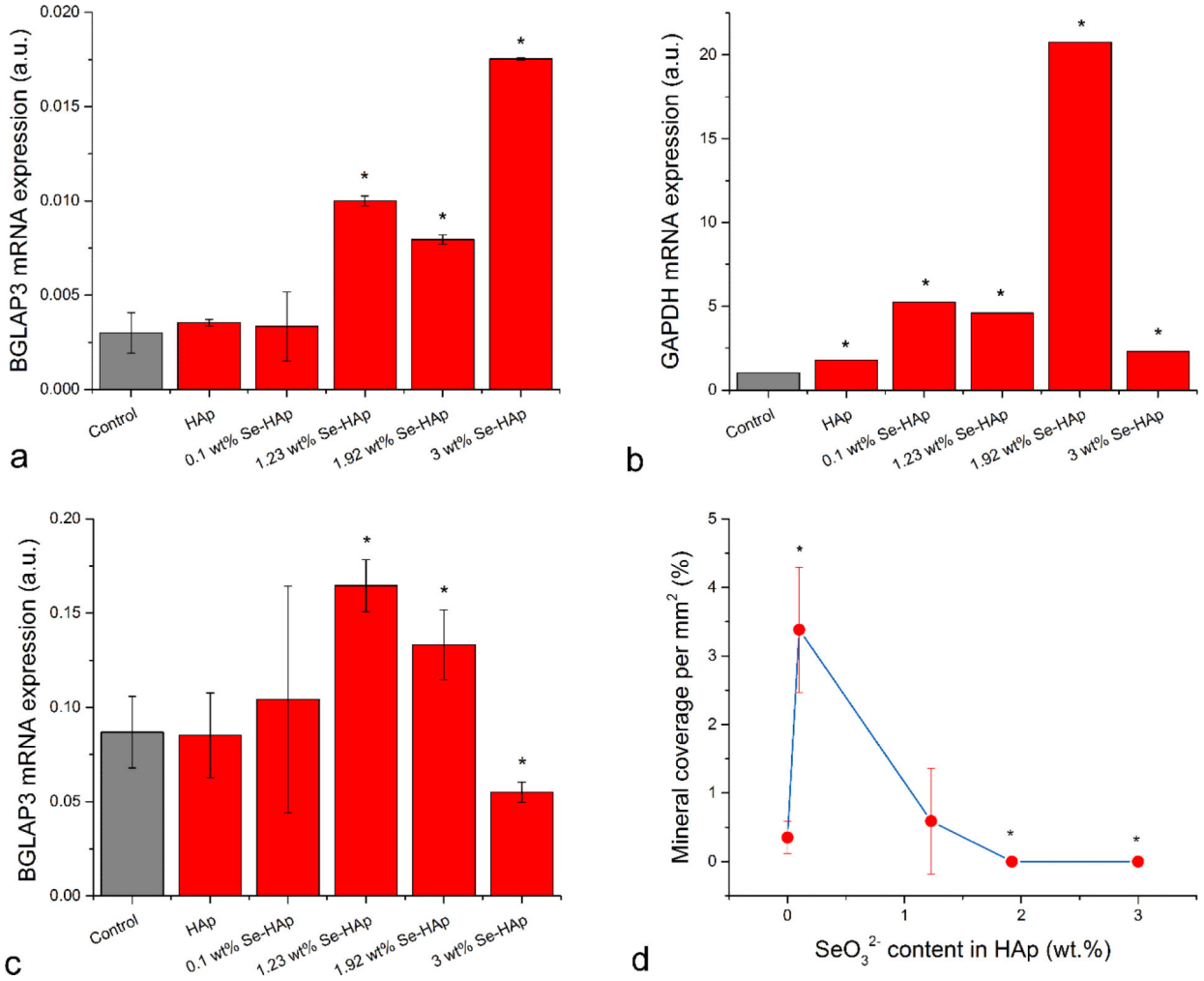

Fig.13.

Absolute mRNA expression of BGLAP3 (a) and GAPDH (b) normalized to the expression of GAPDH in control cell population for differentiated MC3T3-E1 cells treated with different Se-HAp particles. (c) mRNA expression of BGLAP3 relative to the expression of β-actin in differentiated MC3T3-E1 cells treated with different Se-HAp particles. (d) Mineral coverage per mm^2 of surface seeded with MC3T3-E1 pre-osteoblastic cells as a function of the weight percentage of selenite in annealed Se-HAp synthesized by co-precipitation. Bars and error bars represent averages and standard deviations, respectively. Standard deviation is invisible to the eye in (b). Data points statistically significantly higher or lower ($p < 0.05$) compared to the control are marked with an asterisk.

Table 1

Crystallographic parameters of annealed HAp and Se-HAp containing the maximal concentration of selenite ions for different synthesis conditions.

HAp system	d_{300} (Å)	d_{002} (Å)	Lattice parameter *a* (Å)	Lattice parameter *c* (Å)
HAp	2.719	3.437	9.419	6.874
Se-HAp	2.717	3.431	9.412	6.862